

Robustness of momentum-indirect interlayer excitons in MoS₂/WSe₂ heterostructure against charge carrier doping

Ekaterina Khestanova^{1*}, Tatyana Ivanova², Roland Gillen³, Alessandro D'Elia⁴, Oliver Nicholas Gallego Lacey⁴, Lena Wysocki⁴, Alexander Grüneis^{4,5}, Vasily Kravtsov², Wlodek Strupinski⁶, Janina Maultzsch³, Viktor Kandyba⁷, Mattia Cattelan^{7,8}, Alexei Barinov⁷, José Avila⁹, Pavel Dudin⁹, Boris V. Senkovskiy^{4*}

¹*ICFO-Institut de Ciències Fòniques, The Barcelona Institute of Science and Technology, Castelldefels (Barcelona) 08860, Spain*

²*School of Physics and Engineering, ITMO University, 197101 Saint Petersburg, Russia*

³*Department Physik, Friedrich-Alexander-Universität Erlangen-Nürnberg, Staudtstraße 7, 91058 Erlangen, Germany*

⁴*II. Physikalisches Institut, Universität zu Köln, Zùlpicher Straße 77, 50937 Köln, Germany*

⁵*Institut für Festkörperelektronik, Technische Universität Wien, Gußhausstraße 25-25a, 1040 Wien, Austria*

⁶*Faculty of Physics, Warsaw University of Technology, 00-662 Warsaw, Poland*

⁷*Elettra-Sincrotrone Trieste S.C.p.A., Basovizza, 34149 Trieste, Italy*

⁸*Department of Chemical Sciences, University of Padova, Via F. Marzolo 1, 35131 Padova, Italy*

⁹*Synchrotron SOLEIL, Université Paris-Saclay, L'Orme des Merisiers Saint-Aubin, Gif sur Yvette, France*

Abstract

Monolayer transition-metal dichalcogenide (TMD) semiconductors exhibit strong excitonic effects and hold promise for optical and optoelectronic applications. Yet, electron doping of TMDs leads to the conversion of neutral excitons into negative trions, which recombine predominantly non-radiatively at room temperature. As a result, the photoluminescence (PL) intensity is quenched. Here we study the optical and electronic properties of a MoS₂/WSe₂ heterostructure as a function of chemical doping by Cs atoms performed under ultra-high vacuum conditions. By PL measurements we identify two interlayer excitons and assign them to the momentum-indirect Q- Γ and K- Γ transitions. The energies of these excitons are in a very good agreement with *ab initio* calculations. We find that the Q- Γ interlayer exciton is robust to the electron doping and is present at room temperature even at a high charge carrier concentration ($\sim 10^{13}$ cm⁻²). Submicrometer angle-resolved photoemission spectroscopy (μ -ARPES) reveals charge transfer from deposited Cs adatoms to both the upper MoS₂ and the lower WSe₂ monolayer without changing the band alignment. This leads to a small (~ 10 meV) energy shift of interlayer excitons. Robustness of the momentum-indirect interlayer exciton to charge doping opens up an opportunity of using TMD heterostructures in light-emitting devices that can work at room temperature at high densities of charge carriers.

Introduction

Monolayer transition metal dichalcogenides (TMDs) are direct band gap semiconductors with multi-valley electronic band structure and strong light-matter coupling. These properties give rise to a variety of electron-hole pair excitations (excitons) that are stable at room temperature.¹ When monolayer TMDs are stacked in van der Waals heterostructures with type-II band alignment, electrons and holes reside in different layers and interlayer excitons (ILEs) emerge. Such ILEs demonstrate extremely long lifetime, large valley polarization and coherence, necessary for valleytronics applications.²⁻⁴ It was demonstrated that application of external electric fields provides control over properties of ILEs: their intensity and photon energy,² valley polarisation,^{3,5} and flux.⁶ Such versatile tunability of ILEs makes TMDs heterostructures promising for designing optoelectronic devices such as light-emitting diodes (LEDs), solar cells, photodetectors, energy conversion and storage devices. First, an ILE in MoS₂/WSe₂ heterostructures fabricated on SiO₂ substrates was observed with light emission at around 1.6 eV,⁶⁻⁸ and the electrical control of its diffusion in a sample encapsulated between hexagonal boron nitride (hBN) layers was also demonstrated.⁶ Experimental data and calculations suggest that this ILE is momentum-indirect, i.e. an electron in MoS₂ and a hole in WSe₂ have different wavevectors.⁸ It was proposed that this ILE consists of an electron residing in the K valley of MoS₂ and a hole residing in the Γ valley of WSe₂.⁸ Further, a momentum-direct ILE, coupling the K valleys of MoS₂ and WSe₂, was found in MoS₂/WSe₂ heterostructure at around 1 eV.⁹ Interestingly, in a very similar system – hBN-encapsulated MoS₂/WS₂, two momentum-indirect ILEs were observed.¹⁰ These ILEs are associated with two conduction band (CB) valleys of MoS₂ located in the K and Q points and the

valence band (VB) valley of WS_2 at the Γ point.¹⁰ The hBN encapsulation plays an important role in this finding. For example, for a non-encapsulated MoS_2/WS_2 heterostructure on SiO_2 , the contribution of two momentum-indirect ILEs cannot be well resolved.¹¹ These results suggest further investigation of the $\text{MoS}_2/\text{WSe}_2$ system, in which two types of momentum-indirect ILEs can be also present.

Besides the origin of ILEs in TMD heterostructures, another open question is the impact of charge doping on the ILE emission. This is an important question not only from a fundamental but also from an applied point of view. For devices that require both light emission and charge transport, it is important to maintain the radiative efficiency at an increased charge carrier densities. For example, conductivity and the charge carrier mobility in TMDs can be increased by charge doping.¹² However, increased charge carrier concentration in TMD monolayers leads to the conversion of neutral excitons into trions, which have long radiative and short non-radiative lifetimes.¹³ In the case of electron doping, negative trions, composed of two electrons and one hole, will appear. Here, the main mechanism responsible for non-radiative recombination is the Auger process, where the energy of electron-hole recombination is transferred to the third particle (i.e. an electron in negative trions).¹³⁻¹⁵ Thus, Auger recombination dramatically decreases the PL quantum yield, which complicates the use of TMDs as optical active elements at a high concentration of charge carriers. Nevertheless, the impact of electron doping on PL of momentum-indirect ILEs involving different valleys in CB might be different. To answer these questions, we explore a high-quality $\text{MoS}_2/\text{WSe}_2/\text{hBN}$ van der Waals heterostructure and find two momentum-indirect ILEs. To understand the origin of these ILEs, we perform *ab initio* calculations of optical tran-

sitions in MoS₂/WSe₂ system. We investigate the effect of electron doping on the electronic and optical properties of the MoS₂/WSe₂ heterostructure using the deposition of Cs atoms *in situ*. Ultra-high-vacuum (UHV) PL spectroscopy reveals that the Q-Γ exciton is robust to the electron doping and is emitting light even at high charge carrier concentration ($\sim 10^{13} \text{ cm}^{-2}$) at room temperature. Using the spatially-resolved angle-resolved photoemission spectroscopy with sub-micron spot (μ -ARPES), we find that the deposition of Cs has a minor impact on the VB alignment in MoS₂/WSe₂ heterostructure. This is due to the intercalation of Cs in the van der Waals gap, which leads to equal charge distribution between the TMD monolayers. This explains the minor shift of ILEs in the MoS₂/WSe₂ system upon Cs doping. The robustness of momentum-indirect ILEs to the charge doping paves the way towards the design of novel optoelectronic devices based on TMD heterostructures with combined effective light emission and improved charge transport properties at high charge carrier concentrations.

Sample fabrication and characterization

PL and μ -ARPES studies were performed on similar samples fabricated by the deterministic transfer technique.¹⁶ The MoS₂/WSe₂ heterobilayers were assembled layer by layer on hBN flakes placed on epitaxial bilayer graphene grown on SiC. The advantage of such a substrate is that hBN is an atomically flat and pure insulator (in contrast to SiO₂), while graphene provides the electrical conductivity (through the TMD edges lying outside the hBN flake), necessary for μ -ARPES measurements. The hBN flake also ensures the absence of charge transfer between the TMD heterostructure and graphene in PL measurements. To minimize organic residues, we ex-

foliated monolayer TMDs on ultraviolet-ozone cleaned polydimethylsiloxane (PDMS) stamps.¹⁷ Post-transfer thermal annealing of the TMDs heterostructure is an important step to provide strong interlayer coupling.¹⁸ Our samples were annealed in UHV at 250 °C for 3 hours. For further details see Supplementary Information S1.

Fig. 1 (a) illustrates the MoS₂/WSe₂ heterostructure on hBN on bilayer graphene/SiC. The optical image of the sample with indicated edges of the MoS₂ and WSe₂ monolayers is shown in Fig. 1 (b). The monolayers were not perfectly aligned. The twist angle between TMD monolayers was varying within 5° as determined using the second-harmonic generation (SHG) measurements (see Supplementary Information, Fig. S2). Our heterostructures are quite large – several tens of microns, which allows us to probe and compare different points on the sample. The atomic force microscopy (AFM) measurements shown in Fig. 1 (c, d) reveal the surface topography. The exfoliated flakes follow the characteristic atomically flat terraces of hexagonal SiC(0001) with epitaxial bilayer graphene. UHV annealing leads to the aggregation of contaminants trapped between the layers into the bubbles (or blisters). These bubbles are also visible in optical microscope and we select the bubble-free regions to measure Raman and PL spectra with the laser spot of 1 μm. AFM reveals the height of MoS₂/WSe₂ heterobilayer of ~ 1.5 nm (Supplementary information, Fig. S3), indicating the absence of organic residues at the interface and the surface.¹⁷

Fig. 1 (e) shows the typical Raman modes of MoS₂ and WSe₂ in the heterostructure region (532 nm laser). The clean interface provides strong interaction between TMD monolayers. Indeed, in Raman spectra measured with a low wavenumber filter (633 nm laser) we observe

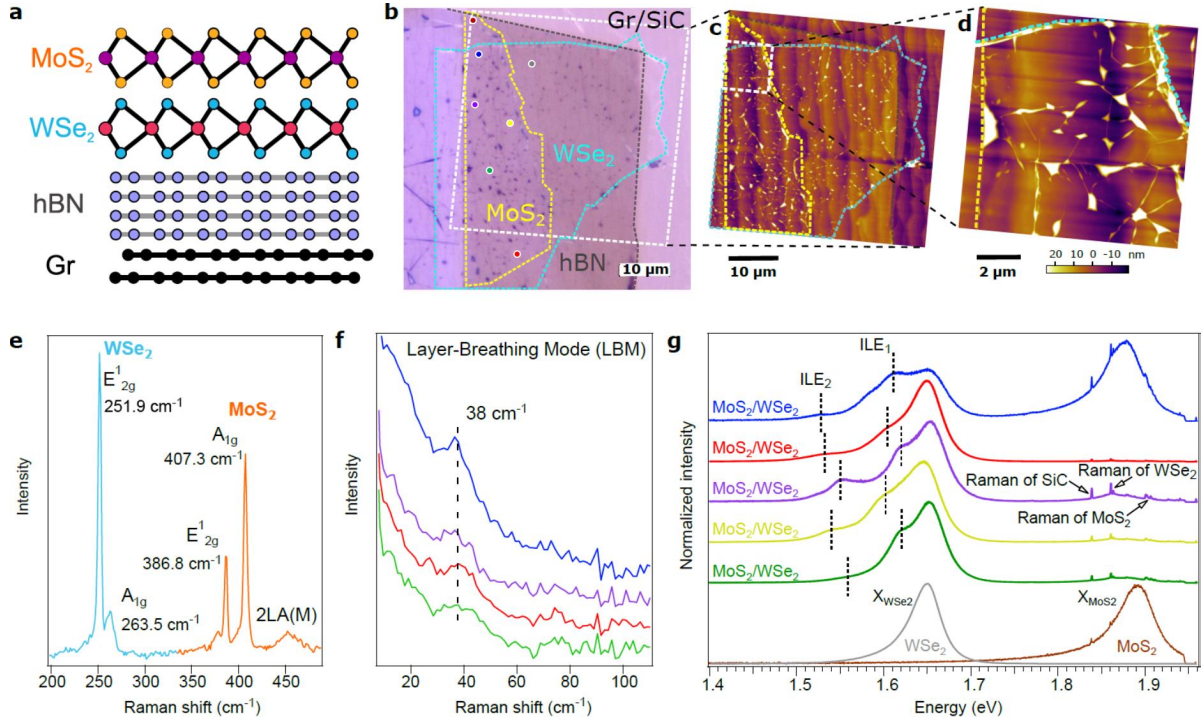


Fig. 1 (a) Illustration of the MoS₂/WSe₂ heterostructure on hBN on epitaxial bilayer graphene. (b) Optical microscope image of the aligned MoS₂/WSe₂ heterostructure. The edges of TMD monolayers are indicated. The white dashed line shows the area where the AFM image was measured. The coloured dots indicate the positions of the laser during measurements shown in Fig.1 (g). (c) AFM topography image of the region outlined by the white dashed line in the panel b. (d) Zoomed-in AFM topography image of the region outlined by the white dashed line in the panel c. (e) Raman spectrum of the heterostructure measured with a 532 nm laser. Vibrational modes of MoS₂ and WSe₂ are indicated. (f) Low-frequency Raman spectra of the heterostructure measured at different points with a 633 nm laser. LBM mode at 38 cm⁻¹ is indicated. (g) PL spectra of the heterostructure measured at room temperature at different points in the bubble-free regions using a 633 nm laser. In addition to the PL peaks from intralayer excitons of MoS₂ and WSe₂, two low-energy features are observed, designated as ILE₁ and ILE₂. The spectra of the individual monolayers are shown at the bottom for reference.

layer-breathing mode (LBM), Fig. 1 (f). This mode arises from the out-of-plane vibration of two monolayers when they are in close proximity. The frequency of the LBM mode (38 cm^{-1}) is comparable to that measured on a heterostructure fabricated from chemically grown TMDs on SiO_2 (35 cm^{-1}).¹⁹ The small difference in frequency might be related to the different substrates or slightly different twist angles. When the laser spot is directed into the bubble, the LBM mode is absent due to weak interlayer coupling in these areas, the signal from the individual monolayers dominates the PL spectra and the ILE peaks, discussed below, are vanishing. These facts allow us to exclude the contribution of bubbles to the PL spectra. Fig. 1 (g) shows the PL spectra measured at room temperature in air in different bubble-free regions of the sample. One can identify the PL peak of MoS_2 at 1.88 eV. This peak is composed of intralayer neutral exciton and negatively charged trion (which manifests itself in the asymmetry of the PL peak towards lower energies).^{20,21} The PL of MoS_2 is suppressed in most of the assessed points due to the interlayer charge transfer in a type-II TMD heterostructure.^{2,7,22} The PL peak at 1.65 eV is the intralayer exciton of WSe_2 , later referred to as X_{WSe_2} . The energy of the momentum-direct K-K exciton in $\text{MoS}_2/\text{WSe}_2$ system is in the infrared range.⁹ Other multi-particle exciton complexes, which may appear energetically below the X_{WSe_2} , such as trions, biexcitons, defect bound excitons, moiré excitons can be observed only at cryogenic temperatures.^{23–29} Consequently, the PL peaks that are observed only in the heterostructure region at room temperature and whose energy is just below the X_{WSe_2} peak should be attributed to the momentum-indirect ILEs. In contrast to the previous studies, revealing a single ILE peak at $\sim 1.6 \text{ eV}$ in the $\text{MoS}_2/\text{WSe}_2$ heterostructures on SiO_2 ,^{6,8,30} we clearly observe two peaks – at $\sim 1.61 \text{ eV}$ and at $\sim 1.55 \text{ eV}$, and denote them as ILE_1 and ILE_2 , respectively. The

energies and intensities of the two ILEs peaks slightly vary from point to point and from sample to sample (see Supplementary Information, Fig. S1). This can be attributed to the variations of interlayer twist angle, interlayer spacing and doping.

***In situ* chemical doping and UHV PL studies**

To avoid the effect of air adsorbates (e.g. water molecules, oxygen, hydrocarbons) and to investigate the impact of chemical doping on intrinsic optical properties of MoS₂/WSe₂ system, we performed PL studies in UHV conditions. For this we used a unique UHV optical setup for PL and Raman studies.³¹⁻³⁴ Fig. 2 (a) shows the evolution of the UHV PL spectra of the sample upon deposition of Cs. The Cs dose was calibrated using a quartz crystal microbalance. The measurements show that intralayer excitons (X_{MoS_2} and X_{WSe_2}) and the interlayer exciton ILE₂ are suppressed as the Cs dose increases. The PL of excitons is mainly suppressed due to their conversion to negative trions^{20,35} via electron donation by Cs atoms with the subsequent non-radiative recombination of trions through Auger processes.¹³⁻¹⁵ Moreover, doping increases the dielectric screening of electron-hole Coulomb interaction, and hence reduces the binding energy and the oscillator strength of excitons,³⁶ which in turn lowers the radiative decay rate. In addition, in case of intercalation of Cs into the van der Waals gap, the interlayer distance will be increased and, consequently, the PL intensity will be reduced. After deposition of ~ 1 Å of Cs one can see almost no signal from X_{MoS_2} , X_{WSe_2} and ILE₂ peaks (purple spectrum in Fig. 2 (a)). At the same time, the intensity of the ILE₁ peak is relatively large. Even after increasing the Cs dose to ~ 2 Å, the ILE₁ peak remains clearly visible, while its intensity is reduced by a factor of ~ 3 (light

blue spectrum in Fig. 2(a)). The Cs dosage above 2 Å has much less effect on PL spectra, and we did not observe complete suppression of the ILE₁ peak. Fig. 2 (b) shows the fits of the PL spectra in the pristine and Cs-doped heterostructure. The energies of PL peaks are identified. The full width at half-maximum (FWHM) of these peaks are 19, 21 and 40 meV for X_{WSe₂}, ILE₁ and ILE₂, correspondingly. Such narrow emission lines at room temperature indicate the high quality of our samples.³⁷ This is due to the atomically flat hBN substrate without charge impurities and the absence of unintended functionalization by air adsorbates in UHV conditions. Further evidence of high-quality samples comes from the well-resolved electronic bands in μ -ARPES spectra shown below, since ARPES is a surface-sensitive technique requiring atomically-clean surfaces and interfaces. Interestingly, upon doping, the ILE₁ peak becomes even narrower (lower spectrum in Fig. 2 (b)). The FWHM of ILE₁ is 13 meV at the maximum doping level. This suggests that there is no broadening of ILEs due to the inhomogeneous doping or exciton scattering.

Energies of interlayer excitons

To understand the nature of the observed ILEs, we compare the energy position of PL peaks with calculations. The energies of the X_{MoS₂}, X_{WSe₂} and ILE₂ peaks (1.9 eV and 1.65 eV, and 1.55 eV, correspondingly) agree very well with the reported *ab initio* calculations of intralayer MoS₂ and WSe₂ K-K transitions and interlayer K- Γ transition, respectively.⁹ Previously,⁸ for the heterostructures on SiO₂ substrate, the ILE₂ peak was not observed, and the K- Γ transition was assigned to the peak at \sim 1.6 eV, which we designated as ILE₁.

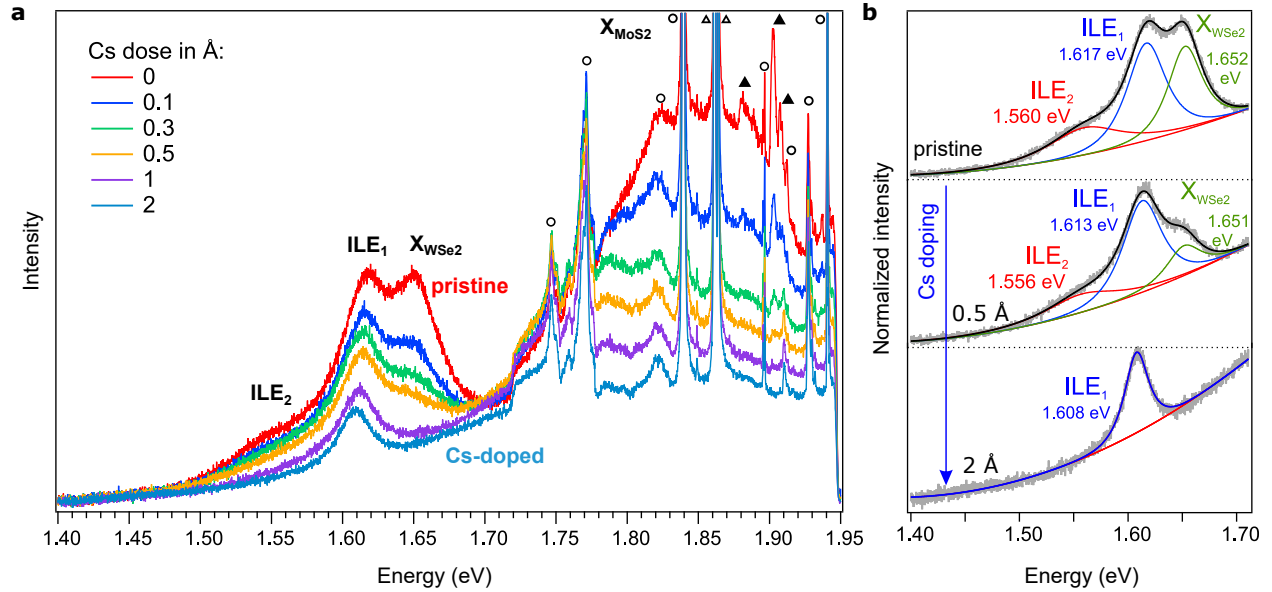


Fig. 2 (a) UHV PL spectra of MoS₂/WSe₂ heterostructure on hBN on bilayer graphene/SiC upon Cs doping, room temperature, 633 nm laser. The intralayer and interlayer excitons are indicated as X_{WSe2} and ILE₁, ILE₂, correspondingly. The PL intensity of MoS₂ and WSe₂ (labeled as X_{MoS2} and X_{WSe2}), as well as of intralayer ILE₁ exciton is completely suppressed as the Cs dose is increased to ~ 2 Å. At the same time, the intensity of the ILE₁ feature is suppressed by ~ 3 times compared to the pristine sample. Raman peaks from SiC, MoS₂ and WSe₂ are indicated by open circles, filled triangles and open triangles, respectively. (b) Fits of the PL spectra of the pristine and doped heterostructure by mixed Gaussian-Lorentzian (0.2/0.8) function. The energies of the peaks are indicated.

To shed further light on the nature of ILE_1 and ILE_2 , we performed additional theoretical calculations to estimate the binding energies of the momentum-indirect K- Γ , Q- Γ and Q-K excitons combining the solution of the Bethe-Salpeter Equation (BSE) with density functional theory calculations. We refer to the method section and the Supplementary Information for details on the computational approach. Figure 3 (a) shows the obtained electronic band gaps, exciton binding energies and predicted excitonic peak positions of the direct K-K and the three candidate indirect transitions.

For the interlayer K-K transitions, we predict a binding energy and a peak position of 310 meV and 1 eV, respectively, in good agreement with experiments⁹ and previous theoretical works.^{38,39} According to our calculations, a Q-K exciton with binding energy 220 meV should appear at an energy of about 1.3 eV, however, to the best of our knowledge, it has not been observed experimentally so far. K- Γ and Q- Γ excitons involve the same hole valley at Γ , but different electronic valleys with different corresponding effective masses. Therefore, the binding energies for the K- Γ and Q- Γ excitons may also be different. Nevertheless, we find very similar binding energies for these excitons (Fig. 3 (a)), and the difference in PL peak positions E_{ILX} is determined by the difference in electronic band gaps, such that $E_{ILX}^{Q-\Gamma} > E_{ILX}^{K-\Gamma}$. This would suggest that ILE_2 indeed should be assigned to a K- Γ exciton, while ILE_1 is the Q- Γ transition. The energies of the ILE_1 and ILE_2 peaks (1.61 eV and 1.55 eV) are very close to the calculated values of $E_{ILX}^{Q-\Gamma} = 1.69$ eV and $E_{ILX}^{K-\Gamma} = 1.45$ eV, correspondingly. We note that our DFT calculations likely overestimate the energy difference between the K and Q conduction band minima compared to more sophisticated GW calculations, as observed in lattice-matched MoSe₂/WSe₂ heterostructures.³⁹

According to Fermi's golden rule, the exciton PL intensity is proportional to the square of the transition matrix element, which, in turn, depends on the overlap between electron and hole wave functions. Momentum-indirect ILEs in type-II TMD heterostructures involve strongly hybridized valleys with large interlayer orbital overlap, and therefore, have significant PL intensity.^{8,10,11} To compare the Q- Γ and K- Γ ILEs, we should have to look at the wavefunctions of electrons in Q and K valleys of MoS₂ and a hole in Γ valley of WSe₂. Fig. 3 (b)-(d) demonstrates a certain delocalization of an electron in Q (panel (c)) and a hole in Γ (panel (b)), while this delocalization is completely absent for electrons in the K points of the sublayers (panel (d) for the MoS₂ K point). The reason for this is that both Q and Γ valleys in the MoS₂/WSe₂ heterostructure are hybridized, as shown by the color code in Fig. 4 (a). This hybridization is possible thanks to the energy overlap of MoS₂ and WSe₂ orbitals in the Γ valley of VB and the Q valley of CB (see Supplementary Information, Fig. S5 (b)). Moreover, the corresponding MoS₂ and WSe₂ orbitals have similar character – predominantly out-of-plane (d_{z^2}) in VB Γ -valley and mixed in-plane ($d_{x^2-y^2}$ and d_{xy}) and out-of-plane in CB Q-valley.⁴⁰⁻⁴³ The increased electron-hole wavefunction overlap for the Q- Γ transition might explain the brightness of the ILE₁ peak in PL spectra compared to the weaker intensity of ILE₂ (corresponding electron-hole wavefunction overlap for the K- Γ transition).

Let us discuss the difference between two momentum-indirect interlayer exciton Q- Γ and K- Γ with respect to the response to electron doping. Upon doping, donated electrons first populate the CB minimum, which is located in the K valley of MoS₂. The Q valley gets populated only at charge carrier density larger than $2 - 6 \times 10^{13} \text{ cm}^{-2}$.^{44,45} As will be seen from our μ -ARPES data shown below, we reach the electron densities when only the K valley gets populated. Additional

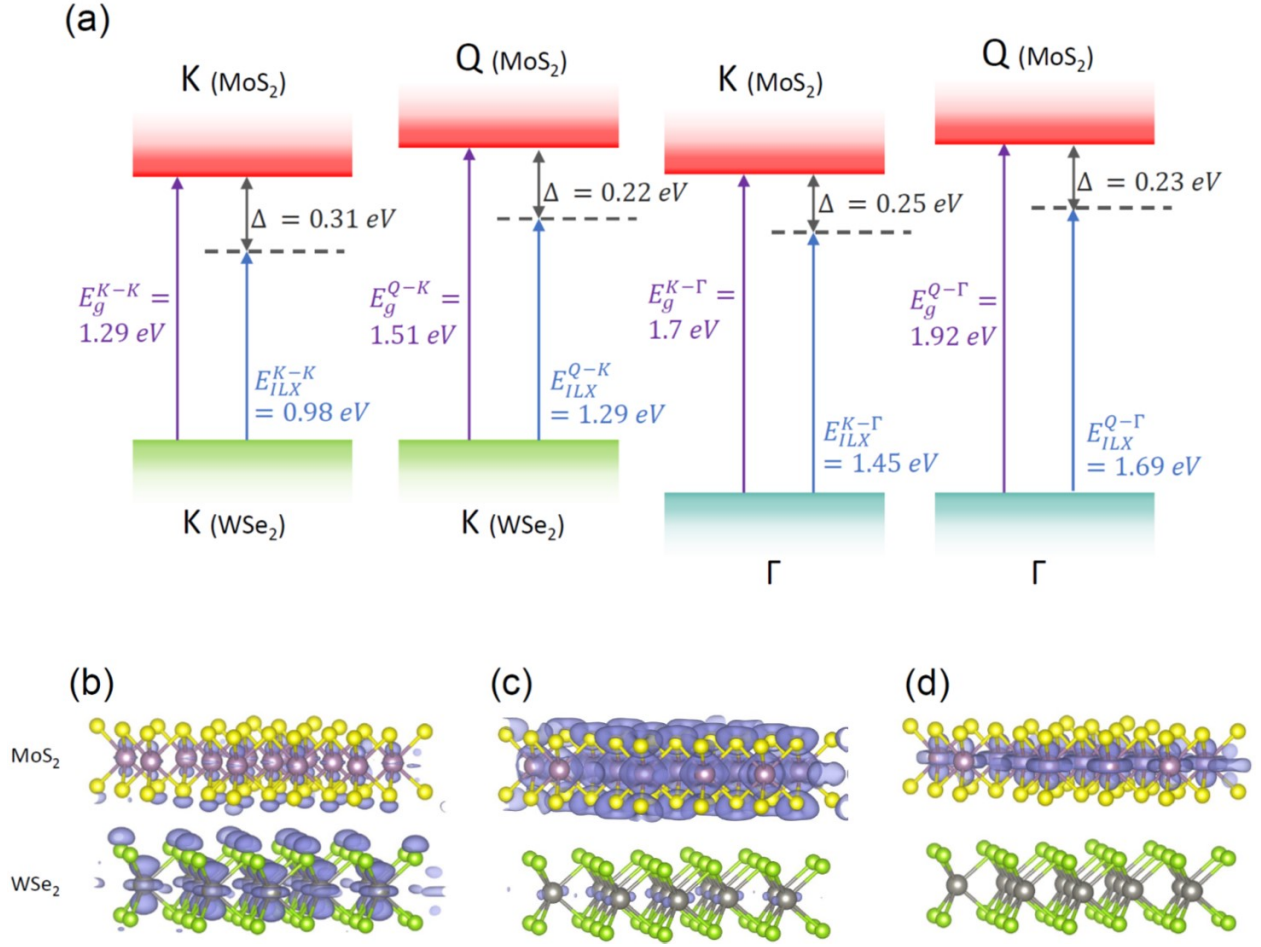


Fig. 3 (a) Schematic illustration of relevant direct and indirect transitions between Γ , Q and K points from our *ab initio* simulations. In case of K and Q, brackets indicate the sublayers the band edges belong to. E_g are the *electronic band gaps* from calculation with the HSE12 functional (see Supplementary Information S4). Dashed lines indicate energy positions of bound excitons with binding energies Δ obtained from solution of the excitonic Bethe-Salpeter Equation (BSE). (b) Plot of the hole wavefunction of the local VBM at the Γ point of the heterostructure. (c) Electron wavefunction corresponding to the Q point local CBM of the MoS₂ sublayer. Notice a small spillover of the wavefunction into the WSe₂ layer. (d) Plot of the electron wavefunction at the K point conduction band minimum (CBM) of the MoS₂ sublayer, which also is the global CBM of the heterostructure.

charge carriers at the K valley lead to the conversion of K- Γ interlayer excitons (ILE_2) into the trions with two electrons in the K (and/or K') valley and a hole in the Γ valley. Let us denote them as KK- Γ trions. As discussed above, the exciton-to-trion conversion and subsequent non-radiative recombination of trions is the most common mechanism of exciton suppression in TMDs upon charge carrier doping. Fig. 4 (b) illustrates the formation of KK- Γ and QK- Γ trions upon electron doping. For simplicity, we show only the KK- Γ singlet trion, but there also should be a KK'- Γ trion and the respective triplet variants with very similar energies, which might appear upon doping. A negative trion can be considered as two excitons sharing the same hole. That is, the QK- Γ trion having two electrons in the Q and K valleys is the combination of Q- Γ and K- Γ excitons. Our calculations demonstrate that the K- Γ ILE has a lower energy than the Q- Γ ILE. Therefore, the KK- Γ trion should also have a lower energy than the QK- Γ trion. Since trions are fermionic states following the Pauli exclusion principle, the lowest energy ground state corresponding to the KK- Γ trion will be populated first. As a result, the Q- Γ excitons are more stable to the conversion into trions than the K- Γ excitons, and, therefore, are more resistant to electron doping. This confirms the experimentally observed stability of the ILE_1 peak in the Fig. 2.

The band alignment and μ -ARPES studies

An important question is the change of ILEs energy upon doping. Deposition of alkali metals on the surface of van der Waals layered materials usually leads to the strong out-of-plane potential difference (Stark effect), with the topmost layers being much more heavily doped than the bottom layers.⁴⁶⁻⁴⁸ If Cs atoms were resting on top of the $\text{MoS}_2/\text{WSe}_2$ heterostructure, the top MoS_2

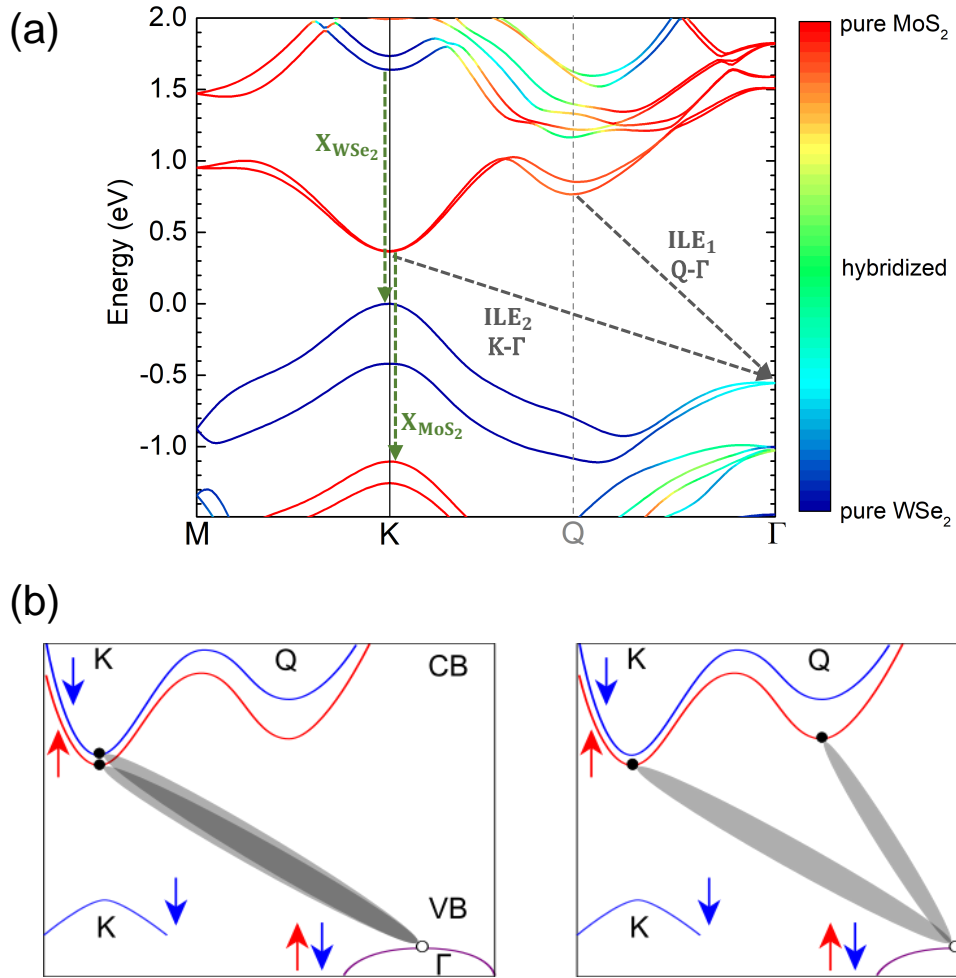


Fig. 4 (a) DFT band structure of a $\text{MoS}_2/\text{WSe}_2$ heterostructure containing one formula unit of MoS_2 and WSe_2 used in our calculations (see Supplementary S4). The interlayer hybridization distribution is shown with the color code. The intralayer X_{MoS_2} and X_{WSe_2} , as well as the momentum-indirect interlayer ILE_1 and ILE_2 transitions are illustrated. We note that the band energies are significantly affected by the strain, while the hybridization reasonably agrees with the results obtained for a strain-free heterostructure. (b) Schematic of the $\text{KK-}\Gamma$ and $\text{QK-}\Gamma$ triions forming upon electron doping.

monolayer would be much more doped than the bottom WSe₂ monolayer. This would lead to a strong modification of the band alignment, which, in turn, would result in a significant change of the ILEs energy. Our data in Fig. 2 show that the final doping level causes a shift of the ILE₁ peak by only 10 meV. The change in carrier concentration also affects the exciton binding energy and the quasiparticle band gap. Nevertheless, these two renormalization effects usually counteract each other, and the total change in optical band gap is minor.^{49,50} Therefore, small changes in the ILEs energy suggest that the band alignment in the MoS₂/WSe₂ heterostructure should not be strongly affected by Cs doping. To understand this behaviour, we investigate our system by μ -ARPES.

In our experiments we compare MoS₂ monolayer and MoS₂/WSe₂ heterostructure doped by an identical amount of Cs. Fig. 5 summarizes the μ -ARPES data. The optical image of aligned MoS₂/WSe₂ heterostructure on an hBN flake on bilayer graphene/SiC used for the μ -ARPES studies is shown in Fig. 5 (a). The scanning photoemission microscopy (SPEM) image allows identification of the sample location, see Fig. 5 (b). The SPEM image visualizes the integrated photoemission intensity around the K point of MoS₂ and WSe₂. Figs. 5 (c) and (d) show the energy band structure of the monolayer MoS₂ and the MoS₂/WSe₂ heterostructure measured by μ -ARPES on the corresponding sample regions. In the heterostructure region (Fig. 5 (d)), in addition to the MoS₂ bands one can see bands of WSe₂ indicated by the arrows. Specifically, a WSe₂ band appears around the Γ point and two spin-split bands appear with vanishing intensities as the K point is approached. In the heterostructure, the WSe₂ states at the Γ point are more dispersing as compared to the states in monolayer WSe₂, where the topmost band at the Γ point is almost flat (see Supplementary Information, Fig. S3). This is the result of interlayer hybridization with MoS₂ states, also

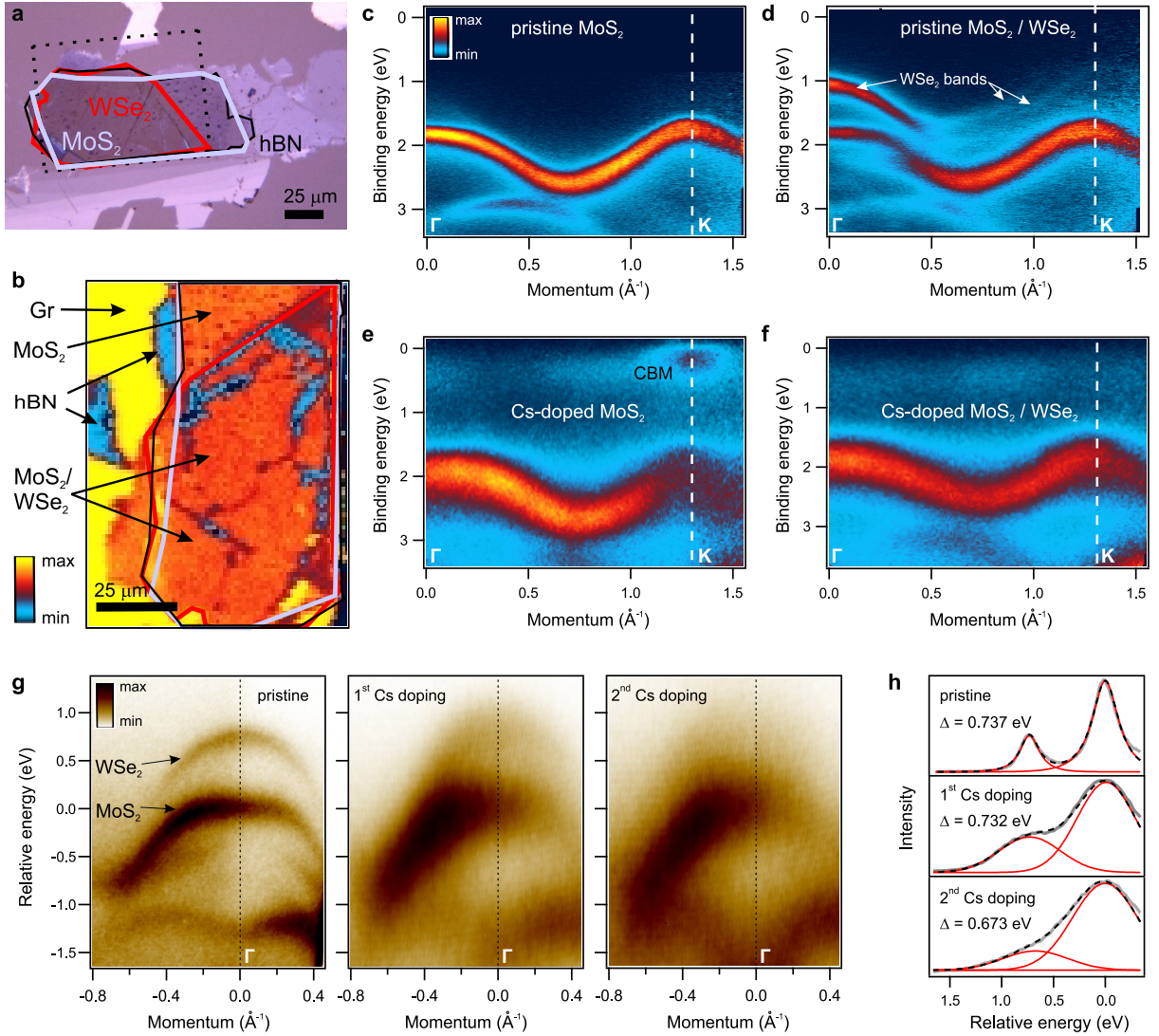


Fig. 5 (a) Optical microscope image of the aligned $\text{MoS}_2/\text{WSe}_2$ heterostructure on hBN on epitaxial bilayer graphene on SiC and (b) its SPEM image, representing the integrated intensity of the μ -ARPES image around the K point. MoS_2 is the upper layer, and WSe_2 is the lower layer. (c, d) Momentum slices of the μ -ARPES data along the K- Γ direction of the (c) monolayer MoS_2 and (d) $\text{MoS}_2/\text{WSe}_2$ regions. The energy bands attributed to the WSe_2 are denoted. (e, f) The same as in panels (c, d) but after Cs doping ($\sim 2 \text{ \AA}$). (g) μ -ARPES spectra of the pristine and doped $\text{MoS}_2/\text{WSe}_2$ heterostructure on hBN/graphite/Si acquired along the K- Γ direction. Each Cs dose was $\sim 1 \text{ \AA}$. The energy is taken relative the MoS_2 band at the Γ point. (h) EDCs from the spectra in panel (g) at the Γ point. The energy difference between the MoS_2 and WSe_2 bands is indicated as Δ .

predicted by our calculations (Fig. 3 (b)). Figs. 5 (e) and (f) demonstrate corresponding spectra after deposition of $\sim 2 \text{ \AA}$ of Cs adatoms on the sample. The monolayer MoS_2 becomes degenerately doped, as we observe the CB states corresponding to the K valley below the Fermi level, Fig. 5 (e). This suggests a doping level of $\sim 10^{13}$ electrons per cm^2 .³⁴ Further deposition of Cs did not result in the appearance of a Q point below the Fermi level, supporting the fact that the PL signal from the Q- Γ ILE was not completely suppressed (Fig. 2), and we are close to the maximum possible Cs doping of our system. At the same time, the $\text{MoS}_2/\text{WSe}_2$ heterostructure is not turned into a metal, since its CB does not cross the Fermi level, Fig. 5 (f). This implies that in the heterostructure the upper MoS_2 layer is less doped compared to the monolayer sample, and a significant amount of charge is transferred to the lower WSe_2 layer. We then performed an experiment with step-by-step deposition of Cs. The obtained high-resolution μ -ARPES spectra are shown in Fig. 5 (g), and the corresponding energy distribution curves (EDCs) at the Γ point are shown in Fig. 5 (h). After the first Cs dose ($\sim 1 \text{ \AA}$), the MoS_2 and WSe_2 bands have large energy broadening, but the energy distance between them (indicated as Δ in Fig. 5 h) is not changed. The second deposition of the same Cs dose leads to the minor reduction of the Δ . Therefore, we can conclude that the Cs doping has a minor impact on the relative energy positions of MoS_2 and WSe_2 bands in the heterostructure. This suggests an equal charge doping of MoS_2 and WSe_2 monolayers, which can occur when Cs atoms are intercalated into the interlayer van der Waals gap. This is also supported by our X-ray photoemission spectroscopy (XPS) data (see Supplementary Information, Fig. S6). A similar behaviour was previously observed by ARPES during the deposition of potassium onto the surface of a bulk MoS_2 crystal.⁵¹ Previous DFT calculations also supported that intercalation

of deposited alkali metals into the van der Waals gap between the topmost TMD monolayers is much more energetically favorable than the adsorption on the surface.⁵¹

It should be noted that in addition to electron doping, which can be implemented in devices, other effects also take place during chemical doping. First, the presence of positive Cs ions can contribute to exciton scattering.⁵² Second, intercalation of alkali metals leads to an increased interlayer distance. Nevertheless, our experimental data suggest that Cs intercalation does not completely suppress the Q- Γ exciton (as occurs in the case of other excitons): its intensity is reduced by ~ 3 times at largest Cs dose of $\sim 2 \text{ \AA}$ (Fig. 2). Concerning the energy position of Q- Γ exciton peak, theory predicts that the increase of interlayer distance from 0.6 nm to 1 nm should reduce the ILE binding energy in MoS₂/WSe₂ heterostructure by about 15 meV.⁵³ This is a small change compared to the two competing factors – the band gap renormalization and the reduction in exciton binding energy due to doping,³⁴ and is comparable with changes that we observe in our data, where the final doping level causes a shift of the ILE₁ peak by only 10 meV.

Conclusions

In conclusion, we fabricated high-quality MoS₂/WSe₂ heterostructures on hBN/graphene/SiC, and characterize their optoelectronic properties and the effect of chemical doping using combination of UHV PL and μ -ARPES techniques. Our PL spectra revealed two interlayer excitons, the energies of which agree very well with our *ab initio* calculations of momentum-indirect K- Γ and Q- Γ optical transitions. The relatively high intensity of the Q- Γ ILE is ascribed to the significant overlap of both

electron and hole wave-functions of the hybridized Q and Γ valleys. To investigate the effect of chemical doping on the ILEs, we performed deposition of Cs atoms onto the MoS₂/WSe₂ system. Room-temperature UHV PL measurements reveal that electron doping induced by Cs leads to the suppression of the emission from both WSe₂ and MoS₂ intralayer excitons and the K- Γ interlayer exciton. In contrast, PL from Q- Γ interlayer exciton is robust to chemical doping, and is preserved even at high electron concentration ($\sim 10^{13}$ cm⁻²). We attribute this to the stability of Q- Γ ILE to the conversion into trions, which recombine non-radiatively at room temperature. Further insight into the interplay between radiative and non-radiative relaxation channels in chemically doped TMD heterostructures can be provided by time-resolved PL measurements. With μ -ARPES we found that upon Cs doping the electronic band alignment is almost not changed. This suggests equal charge doping of both monolayers and intercalation of Cs in the interlayer gap. Two doping-induced effects, quasiparticle band gap renormalization and the reduction of exciton binding energy due to the increased screening, counteract each other. As a result, the energy shift of Q- Γ interlayer exciton upon doping is only 10 meV. The robustness of momentum-indirect interlayer excitons creates a new playground for optical studies of doped TMD heterostructures. This also opens an opportunity to use TMDs in light-emitting devices at a high concentration of charge carriers at room temperature.

Methods

Fabrication of heterostructures MoS₂/WSe₂/hBN heterostructures were fabricated on epitaxial bilayer graphene on silicon carbide (SiC). Using bilayer graphene on SiC as a substrate allows

us to perform both UHV PL and μ -ARPES studies. We exfoliated MoS₂ and WSe₂ monolayers and hBN flakes onto viscoelastic PDMS stamps.¹⁶ The PDMS stamps prior to exfoliation were cleaned with a UV-lamp to minimize organic residues from polymers.¹⁷ The whole cleaning process took 15 minutes. The crystallographic axis (zigzag or armchair) of TMD monolayers on PDMS stamps was determined using the SHG measurements. Then we used a transfer system to create heterostructures layer by layer. First, we've transferred a thin (few tens of nm) hBN flake to the substrate by a PDMS clean stamp. Next, a WSe₂ monolayer was placed on hBN at a temperature of 60°C. After that, we align the bottom WSe₂ layer on substrate with the PDMS stamp on which MoS₂ is located. After alignment, the MoS₂ was transferred on top of WSe₂. Finally, we annealed the samples in high vacuum at 250°C for 3 hours.

PL and Raman measurements PL and Raman characterisation of MoS₂/WSe₂ samples was performed at room temperature in the back-scattering geometry using Renishaw inVia setup with 633 nm and 532 nm lasers. We adjust the laser power below 1 mW to not induce degradation of samples during the measurements. The laser spot size was about 1 μ m. The low wavenumber Raman data were acquired using the Eclipse filter from Renishaw. UHV PL experiments during Cs doping were performed at room temperature using the same commercial setup with the laser light aligning in a home-built optical chamber.^{31,54} In our UHV PL setup we installed a motorized beam splitter with a mini camera and a light source. This allowed us to focus the laser onto the interesting sample area and accumulate PL spectra from the same sample spot after each Cs dose. Cs deposition was performed in the same chamber using a SAES getter. The Cs dose was controlled by a quartz crystal microbalance sensor.

μ -ARPES experiments μ -ARPES experiments were performed using synchrotron radiation facilities – Spectromicroscopy beamline at ELETTRA (data presented in Fig. 5 c-f) and ANTARES beamline at SOLEIL (Fig. 5 g,h). In all experiments Cs was deposited on the sample at room temperature. The samples were aligned using the ARPES band dispersion maps to measure along the Γ -K direction. The data from the Spectromicroscopy beamline were measured with the photon energy of 27 eV at 40 K and a beam size of 0.6 μm . The data from the ANTARES beamline were measured with the photon energy of 100 eV at 80 K and a beam size of 0.7 μm . Before the measurements the samples were annealed at 250°C – 300°C for 3 – 6 hours. The Cs deposition was also controlled by a quartz crystal microbalance sensor.

Computational methods To predict exciton peak energies despite the large lattice mismatch, we followed the two-pronged approach previously reported in Ref. ⁹: To obtain the relevant electronic band energies and band gaps, we built a nearly strain-free supercell (<0.05% strain) with a 16.1° twist angle between the MoS₂ and the WSe₂ layers. We used the QUANTUM Espresso suite ⁵⁵ and the PBE+D3 exchange-correlation (XC) approximation to optimize the atomic positions and interlayer distances, while keeping the lattice constant fixed at the average of the lattice constants of the isolated systems. The HSE12 XC functional ⁵⁶ was then used to derive the electronic band energies of interest. Spin-orbit interaction was fully included in the calculation of the electronic structure. The exciton binding energies were calculated using a minimal unit cell containing one formula unit of both MoS₂ and WSe₂, where the individual layers were strained by about 2%. Based on the electronic structure obtained from DFT calculations, we used a modified version of the YAMBO code ^{57,58} to calculate the binding energies of direct and indirect excitons of interest

from solution of the excitonic Bethe-Salpeter Equation. The excitonic transition energies were then estimated from a combination of the electronic band gaps from HSE12 calculations and the exciton binding energies. We refer to section 4 of the Supplementary Information for details on the computational parameters used for the DFT and BSE calculations.

Data availability

The datasets generated during and/or analysed during the current study are available from the corresponding authors on reasonable request.

Supplementary information

Supplementary Information: Additional experimental details, including sample preparation and characterization methods; Computation methods and details.

Competing Interests The authors declare no competing interests.

Funding Sources B.V.S. acknowledges DFG project SE2575/4-1 'Engineering the electronic band structure of transition metal dichalcogenide heterostructures in device geometries'. A.D., O.N.G.L., B.V.S. and A.G. acknowledge support through the CRC 1238 within project A01 and the ERC grant no. 648589 'SUPER-2D'.

Correspondence Correspondence and requests for materials should be addressed to EK and BS (email: e.khestanova@gmail.com, senkovskiy@ph2.uni-koeln.de).

References

1. Mak, K. F. & Shan, J. Photonics and optoelectronics of 2D semiconductor transition metal dichalcogenides. Nat. Photonics **10**, 216–226 (2016).
2. Rivera, P. et al. Observation of long-lived interlayer excitons in monolayer MoSe₂–WSe₂ heterostructures. Nat. Commun. **6**, 6242 (2015).
3. Rivera, P. et al. Valley-polarized exciton dynamics in a 2D semiconductor heterostructure. Science **351**, 688 LP – 691 (2016).
4. Miller, B. et al. Long-Lived Direct and Indirect Interlayer Excitons in van der Waals Heterostructures. Nano Lett. **17**, 5229–5237 (2017).
5. Ciarrocchi, A. et al. Polarization switching and electrical control of interlayer excitons in two-dimensional van der Waals heterostructures. Nat. Photonics **13**, 131–136 (2019).
6. Unuchek, D. et al. Room-temperature electrical control of exciton flux in a van der Waals heterostructure. Nature **560**, 340–344 (2018).
7. Fang, H. et al. Strong interlayer coupling in van der Waals heterostructures built from single-layer chalcogenides. Proc. Natl. Acad. Sci. U.S.A. **111**, 6198–202 (2014).
8. Kunstmann, J. et al. Momentum-space indirect interlayer excitons in transition-metal dichalcogenide van der Waals heterostructures. Nat. Phys. **14**, 801–805 (2018).
9. Karni, O. et al. Infrared Interlayer Exciton Emission in MoS₂/WSe₂ Heterostructures. Phys. Rev. Lett. **123**, 247402 (2019).

10. Okada, M. et al. Direct and Indirect Interlayer Excitons in a van der Waals Heterostructure of hBN/WS₂/MoS₂/hBN. ACS Nano **12**, 2498–2505 (2018).
11. Kiemle, J. et al. Control of the orbital character of indirect excitons in MoS₂/WS₂ heterobilayers. Phys. Rev. B **101**, 121404 (2020).
12. Baugher, B. W. H., Churchill, H. O. H., Yang, Y. & Jarillo-Herrero, P. Intrinsic Electronic Transport Properties of High-Quality Monolayer and Bilayer MoS₂. Nano Lett. **13**, 4212–4216 (2013).
13. Lien, D.-H. et al. Electrical suppression of all nonradiative recombination pathways in monolayer semiconductors. Science **364**, 468–471 (2019).
14. Kurzmann, A., Ludwig, A., Wieck, A. D., Lorke, A. & Geller, M. Auger Recombination in Self-Assembled Quantum Dots: Quenching and Broadening of the Charged Exciton Transition. Nano Lett. **16**, 3367–3372 (2016).
15. Carmiggelt, J. J., Borst, M. & van der Sar, T. Exciton-to-trion conversion as a control mechanism for valley polarization in room-temperature monolayer WS₂. Sci. Rep. **10**, 17389 (2020).
16. Castellanos-Gomez, A. et al. Deterministic transfer of two-dimensional materials by all-dry viscoelastic stamping. 2D Mater. **1**, 011002— (2014).
17. Jain, A. et al. Minimizing residues and strain in 2D materials transferred from PDMS. Nanotechnology **29**, 265203 (2018).

18. Tongay, S. et al. Tuning Interlayer Coupling in Large-Area Heterostructures with CVD-Grown MoS₂ and WS₂ Monolayers. Nano Lett. **14**, 3185–3190 (2014).
19. Lui, C. H. et al. Observation of interlayer phonon modes in van der Waals heterostructures. Phys. Rev. B **91**, 165403 (2015).
20. Mak, K. F. et al. Tightly bound trions in monolayer MoS₂. Nat. Mater. **12**, 207–211 (2013).
21. Christopher, J. W., Goldberg, B. B. & Swan, A. K. Long tailed trions in monolayer MoS₂: Temperature dependent asymmetry and resulting red-shift of trion photoluminescence spectra. Sci. Rep. **7**, 14062 (2017).
22. Hong, X. et al. Ultrafast charge transfer in atomically thin MoS₂/WS₂ heterostructures. Nat. Nanotechnol. **9**, 682–686 (2014).
23. Wang, G. et al. Valley dynamics probed through charged and neutral exciton emission in monolayer WSe₂. Phys. Rev. B **90**, 075413 (2014).
24. You, Y. et al. Observation of biexcitons in monolayer WSe₂. Nat. Phys. **11**, 477–481 (2015).
25. Clark, G. et al. Single Defect Light-Emitting Diode in a van der Waals Heterostructure. Nano Lett. **16**, 3944–3948 (2016).
26. Li, Z. et al. Revealing the biexciton and trion-exciton complexes in BN encapsulated WSe₂. Nat. Commun. **9**, 3719 (2018).
27. Paur, M. et al. Electroluminescence from multi-particle exciton complexes in transition metal dichalcogenide semiconductors. at. Commun. **10**, 1709 (2019).

28. Seyler, K. L. et al. Signatures of moiré-trapped valley excitons in MoSe₂/WSe₂ heterobilayers. Nature **567**, 66–70 (2019).
29. Tran, K. et al. Evidence for moiré excitons in van der Waals heterostructures. Nature **567**, 71–75 (2019).
30. Nagler, P. et al. Interlayer Excitons in Transition-Metal Dichalcogenide Heterobilayers. Phys. Status Solidi B Basic Res. **256**, 1900308 (2019).
31. Senkovskiy, B. V. et al. Making Graphene Nanoribbons Photoluminescent. Nano Lett. **17**, 4029–4037 (2017).
32. Hell, M. G. et al. Resonance raman spectrum of doped epitaxial graphene at the lifshitz transition. Nano Lett. **18**, 6045–6056 (2018).
33. Senkovskiy, B. V. et al. Boron-Doped Graphene Nanoribbons: Electronic Structure and Raman Fingerprint. ACS Nano **12**, 7571–7582 (2018).
34. Ehlen, N. et al. Narrow photoluminescence and raman peaks of epitaxial MoS₂ on graphene/Ir(1 1 1). 2D Mater. **6**, 011006 (2018).
35. Mouri, S., Miyauchi, Y. & Matsuda, K. Tunable Photoluminescence of Monolayer MoS₂ via Chemical Doping. Nano Lett. **13**, 5944–5948 (2013).
36. Chernikov, A. et al. Electrical Tuning of Exciton Binding Energies in Monolayer WS₂. Phys. Rev. Lett. **115**, 126802 (2015).

37. Cadiz, F. et al. Excitonic Linewidth Approaching the Homogeneous Limit in MoS₂-Based van der Waals Heterostructures. Phys. Rev. X **7**, 021026 (2017).
38. Latini, S., Winther, K. T., Olsen, T. & Thygesen, K. S. Interlayer Excitons and Band Alignment in MoS₂/hBN/WSe₂ van der Waals Heterostructures. Nano Lett. **17**, 938–945 (2017).
39. Gillen, R. & Maultzsch, J. Interlayer excitons in MoSe₂/WSe₂ heterostructures from first principles. Phys. Rev. B **97**, 165306 (2018).
40. Liu, G.-B., Shan, W.-Y., Yao, Y., Yao, W. & Xiao, D. Three-band tight-binding model for monolayers of group-vib transition metal dichalcogenides. Phys. Rev. B **88**, 085433 (2013).
41. Kang, J., Tongay, S., Zhou, J., Li, J. & Wu, J. Band offsets and heterostructures of two-dimensional semiconductors. Applied Physics Letters **102**, 012111 (2013).
42. Shanavas, K. V. & Satpathy, S. Effective tight-binding model for mX_2 under electric and magnetic fields. Phys. Rev. B **91**, 235145 (2015).
43. Kormányos, A. et al. $k \cdot p$ theory for two-dimensional transition metal dichalcogenide semiconductors. 2D Materials **2**, 022001 (2015).
44. Piatti, E. et al. Multi-Valley Superconductivity in Ion-Gated MoS₂ Layers. Nano Lett. **18**, 4821–4830 (2018).
45. Zhao, P. et al. Electronic and optical properties of transition metal dichalcogenides under symmetric and asymmetric field-effect doping. New J. Phys. **22**, 083072 (2020).

46. Kang, M. et al. Universal Mechanism of Band-Gap Engineering in Transition-Metal Dichalcogenides. Nano Lett. **17**, 1610–1615 (2017).
47. Kim, B. S. et al. Possible electric field induced indirect to direct band gap transition in MoSe₂. Sci. Rep. **7**, 5206 (2017).
48. Ehlen, N. et al. Direct observation of a surface resonance state and surface band inversion control in black phosphorus. Phys. Rev. B **97**, 045143 (2018).
49. Ugeda, M. M. et al. Giant bandgap renormalization and excitonic effects in a monolayer transition metal dichalcogenide semiconductor. Nat. Mater. **13**, 1091–1095 (2014).
50. Gao, S., Liang, Y., Spataru, C. D. & Yang, L. Dynamical Excitonic Effects in Doped Two-Dimensional Semiconductors. Nano Lett. **16**, 5568–5573 (2016).
51. Eknapakul, T. et al. Electronic Structure of a Quasi-Freestanding MoS₂ Monolayer. Nano Lett. **14**, 1312–1316 (2014).
52. Wang, H. et al. Fast exciton annihilation by capture of electrons or holes by defects via Auger scattering in monolayer metal dichalcogenides. Phys. Rev. B **91**, 165411 (2015).
53. Van der Donck, M. & Peeters, F. M. Interlayer excitons in transition metal dichalcogenide heterostructures. Phys. Rev. B **98**, 115104 (2018).
54. Senkovskiy, B. et al. Semiconductor-to-Metal Transition and Quasiparticle Renormalization in Doped Graphene Nanoribbons. Adv. Electron. Mater. **3**, 1600490 (2017).

55. Giannozzi, P. et al. QUANTUM ESPRESSO: a modular and open-source software project for quantum simulations of materials. J. Phys. Condens. Matter **21**, 395502 (2009).
56. Moussa, J. E., Schultz, P. A. & Chelikowsky, J. R. Analysis of the Heyd-Scuseria-Ernzerhof density functional parameter space. J. Chem. Phys **136**, 204117 (2012).
57. Marini, A., Hogan, C., Grüning, M. & Varsano, D. yambo: An *ab initio* tool for excited state calculations. Comp. Phys. Comm. **180**, 1392 (2009).
58. Gillen, R. Interlayer Excitonic Spectra of Vertically Stacked MoSe₂/WSe₂ Heterobilayers. Phys. Status Solidi B Basic Res. **258**, 2000614 (2021).

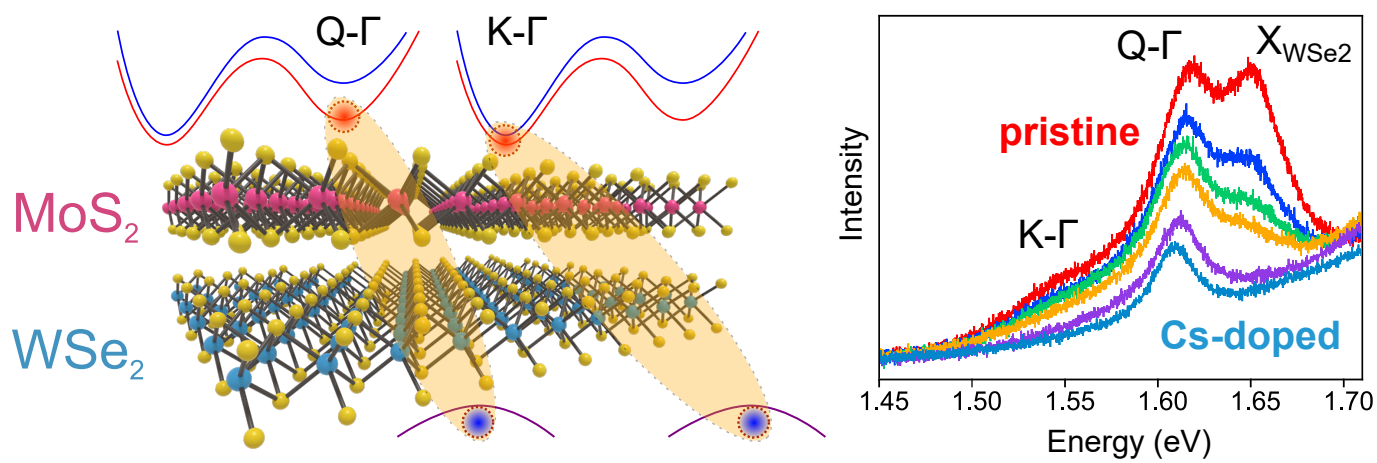


Fig. 6 TOC